

Numerical and Experimental Investigation of Thermal Signatures of Buried Landmines in Dry Soil

F. Moukalled

N. Ghaddar¹

ASME Fellow
e-mail: farah@aub.edu.lb

H. Kabbani

N. Khalid

Faculty of Engineering and Architecture,
American University of Beirut,
Beirut, Lebanon

Z. Fawaz

Ryerson University,
School Aerospace Engineering,
Toronto, Canada, M5B 2K3

This paper reports a numerical and experimental investigation conducted to study the thermal signature of buried landmines on soil surface. A finite-volume-based numerical model was developed to solve the unsteady three-dimensional heat transport equation in dry homogeneous soil with a buried mine. Numerical predictions of soil thermal response were validated by comparison with published analytical and numerical values in addition to data obtained experimentally. Experiments were performed inside an environmental chamber and soil temperatures were measured during cooling, using two measurement techniques, after exposing the soil surface to a radiant heat flux for a specified period. In the first technique, the temporal variation of the surface and internal soil temperatures were recorded using thermocouples. In the second technique, the soil surface temperature was measured using an infrared camera that revealed the thermal signature of the mine. The transient temperature profiles generated numerically agreed with measurements, and the difference between predicted and measured values was less than 0.3°C at both the soil surface and in depth. The accurate matching of numerical and IR images at the surfaces was found to strongly depend on the use of a smaller soil thermal conductivity at the surface than at greater depths. The numerical model was used to predict the dependence of the peak thermal contrast on time, depth, and heating period. The thermographic analysis, when combined with numerical predictions, holds promise as a method for detecting shallowly buried land mines. [DOI: 10.1115/1.2176681]

Keywords: infrared imaging, detection of buried objects, soil thermal response to unsteady surface heating, finite-volume method

1 Introduction

Objects of dissimilar thermal capacitance absorb and release heat at different rates and as such have different infrared (IR) emission characteristics. Therefore, a buried mine heats up and cools down at a rate different from the surrounding soil. This unequal heat transfer rate manifests itself on the surface above the mine through either a higher or a lower soil surface temperature than the surface temperature at a location away from the mine. This variation in temperature is denoted in the literature by thermal signature [1–3] and appears as a thermal contrast in an image taken by an IR camera. Simard [2,3] thoroughly explained the various thermal mechanisms affecting the temperature contrast and related them to the “volume” and “surface” effects. The volume effect results in an alteration of the heat flow due to the presence of the buried mine. The surface effect, which enhances the mine’s signature, is present whenever the soil layer above and around the mine is disturbed (e.g., during the first few weeks after burial). According to numerous studies, IR systems hold promise as a support technology for specific mine-detection situations [4]. The IR technology, which has the key advantage of being passive, could be remotely utilized by aerial search, and could cover a large area in a relatively short time [4]. Infrared thermography is best suited for identifying minefields (global area search), rather than searching for individual mines (local area search) [5]. Nev-

ertheless, a few projects using IR technology aimed at searching for individual mines. One such project involved developing a short range IR system based on an 8–12 μm IR sensor and using neural networks for pattern recognition after segmentation of the image. Reported results indicate that the system is capable of achieving a successful mine-detection rate of 90% [6].

Besides accuracy, it is highly desirable for any potential landmine detection technology to be quick and minimally intrusive. IR technology, as a means for remotely detecting buried landmines, has the potential of combining these desirable features. Since the detection of mines using IR technology is via an image for the soil surface, its degree of success depends on a number of factors including burial depth, soil attributes, moisture content, mine properties, as well as the time of day during when the scanning is performed. Bruschini and Gros [7] assessed the potential of using IR imaging as a landmine detection technology and described its advantages and limitations. They estimated that IR images could spot the presence of an antitank mine at a maximum burial depth of 10–15 cm. Their work also indicated that the results of IR imaging depend heavily on environmental conditions. In a recent paper, Deans et al. [8] presented experimental results of a thermal imaging method using microwave heating to enhance the visibility of buried landmines. They concluded that discovery of mines buried in dry sand is possible up to a burial depth of 2 cm, which differs significantly from the 10–15 cm suggested by Bruschini and Gros [7]. Consequently, the depth at which mines are detectable by an IR sensor strongly depends on the type of mines and the type of soil in which they are buried.

Hermann and Ian [9] investigated experimentally the enhancement of thermal signature of buried landmines using IR sensors through volumetric heating via microwave energy sources. In ad-

¹Corresponding author.

Contributed by the Heat Transfer Division of ASME for publication in the JOURNAL OF HEAT TRANSFER. Manuscript received April 27, 2005; final manuscript received October 25, 2005. Review conducted by Ramendra P. Roy. Paper presented at the 2005 ASME Heat Transfer Summer Conference (HT2005), July 15–22, 2005, San Francisco, California, USA.

dition, the authors presented a one-dimensional model for microwave absorption and heat dissipation by moisture-laden soils with a surrogate buried landmine to model the enhancement of the signature. Mitchell et al. [10] studied the detection of antipersonnel landmines by taking thermal images of the soil surface after spraying it by hot water with an array of jets. The variation in conduction and radiation heat transfer due to the water blocked by the mine and the heating of the mine itself, affected the transient temperature profiles at the soil surface and reflected the presence of the buried mine. Moreover, to reduce the false alarm mitigation (FAM) three quantitative numbers based on gray contrast, temperature gradient, and apparent thermal width were used as indicators. Deepak et al. [11] applied other FAM reduction techniques using three indicators based on circularity, gray scale moment, and reflection symmetry. The study reported reduction in false alarms by factors ranging from four to twelve depending on the mine size.

Recently, Khanafer and Vafai [12] analyzed numerically using the finite-element method effect of surface roughness on thermal signature of buried landmines over a diurnal cycle. In their work, an antitank mine was simulated taking into consideration the effect of its striker mechanism. Khanafer et al. also studied the effect on the soil surface temperature of the mine's outer metal case and its top air gap [13]. Their results show that the thin metal outer case and the top air space of a buried antipersonnel mine have a noticeable effect on the intensity of the landmine signature over a diurnal cycle.

Lopez et al. [1,14] investigated landmine detection numerically and experimentally using, respectively, the finite difference method and infrared technology. Their work [14] consisted of comparing thermal signatures in bare soil generated using a three-dimensional thermal model against signatures obtained from infrared images in order to infer the presence of buried objects. Then, Lopez et al. [14] classified these detected objects into either mine or no-mine categories by solving an inverse heat transfer problem. The analysis of the time evolution of perturbations created by such objects constituted the basis of the classification procedure. Moreover, Sendur and Baertlein [15] conducted a similar study to illustrate the effect of the buried landmines on the surface temperature distribution. Results reported [14,15] good agreement in the measured and predicted thermal contrast at the surface of the soil. However, the difference between the predicted and measured absolute temperatures at the surface [14,15] and in the soil [14] were higher (of $\pm 1^\circ\text{C}$ to $\pm 2^\circ\text{C}$) showing lower matching levels.

From the above, it seems that combining numerical techniques with infrared technology holds a promise with regard to developing a powerful tool for the detection of buried landmines. To this end, the aim of this investigation is to develop a three-dimensional thermal model using a control volume approach to better understand the unsteady heat transport in soil with buried landmines and to predict accurately the soil surface temperature and surface thermal contrast. The model is validated by comparing generated results against available theoretical/numerical values and against measurements taken at controlled ambient conditions in an environmental chamber using both an IR video camera of high thermal resolution and thermocouples embedded in the soil. The temporal variation of the soil surface temperature is generated by subjecting the soil surface to radiant heating for a specified time interval followed by convection cooling. The formulation and validation of the numerical model represent the first step toward the future development of an IR-based tool for detecting buried landmines using both the expected absolute surface temperature and the strength of the thermal contrast as parameters in the mine identification technique.

2 Soil Thermal Model Formulation

A schematic of the physical situation and heat exchange processes is depicted in Fig. 1. The three-dimensional transient heat

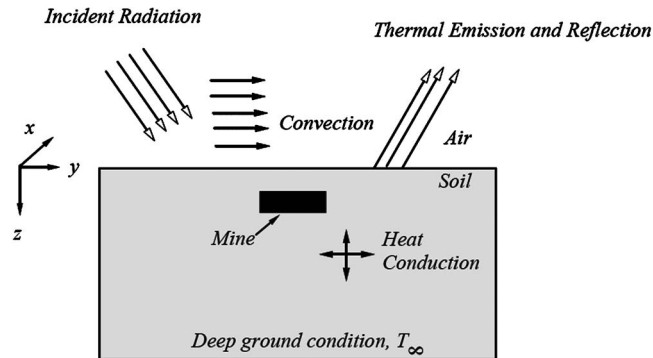


Fig. 1 The soil bed and the embedded mine

conduction equation governs the transport of heat in both soil and mine. Moreover, the target objects buried in it are modeled as isotropic solids. Assuming negligible temporal variation of the moisture content, the resulting governing equations for the soil and the mine can be written as

$$\text{Soil: } \frac{\partial}{\partial t}(\rho c T)_s = \nabla(k \nabla T)_s \quad (1)$$

$$\text{Mine: } \frac{\partial}{\partial t}(\rho c T)_m = \nabla(k \nabla T)_m \quad (2)$$

Where ρ , c , k , and T are the density, specific heat, thermal conductivity, and temperature, respectively. The subscripts s and m refer to soil and mine, respectively. The boundary conditions applicable at the boundaries of the physical domain are given by

$$\text{At the soil surface: } \mathbf{n} \cdot k_s \nabla T_s = q_{\text{net}} \quad (3a)$$

$$\text{At the mine surface: } \mathbf{n} \cdot k_s \nabla T_s = \mathbf{n} \cdot k_m \nabla T_m \quad (3b)$$

$$\text{At vertical boundaries: } \mathbf{n} \cdot k_s \nabla T_s = 0 \quad (3c)$$

$$\text{At the deep soil below the mine: } T_s \rightarrow T_\infty \quad (3d)$$

where \mathbf{n} represents the normal unit vector, T_∞ the deep soil temperature below the buried mine, and q_{net} the net heat flux into the top surface of the soil given by

$$q_{\text{net}} = q_{\text{conv}} + q_{\text{rhs}} - q_{\text{emis}} \quad (4)$$

where q_{conv} is the convective heat transfer between the surface of the soil and the ambient air, q_{rhs} is the incident radiation heat flux on soil surface, q_{emis} is the gray body emission from the soil's surface. In this work, the soil is assumed dry and therefore the latent cooling of the ground caused by evapotranspiration and condensation is neglected. Convective heat transfer between the soil and the surrounding air is expressed as

$$q_{\text{conv}} = Ah(T_\infty - T_s) \quad (5)$$

In Eq. (5), h is the convective heat transfer coefficient at the soil surface and A the surface area. Initially, the soil, ambient air, and mine are considered to be at the same uniform temperature T_∞ . Moreover, assuming the ground surface to behave as a grey body, the long-wave radiation between the soil surface and the room surfaces can be expressed as

$$q_{\text{emis}} = \sigma \varepsilon (T_s^4 - T_\infty^4) \quad (6)$$

where $\sigma = 5.67 \times 10^{-8} \text{ W/m}^2 \text{ K}^4$ is the Stefan-Boltzmann constant, ε is the mean emissivity of the room surfaces, and T_s is the soil's surface temperature. The temperatures of the surfaces surrounding the soil-mine configuration in the environmental chamber are assumed the same as that of the room air temperature.

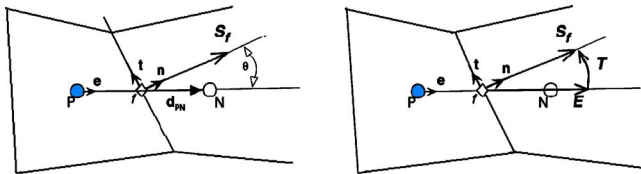


Fig. 2 A schematic showing the treatment of the diffusion term

3 Numerical Analysis

3.1 The Discretization Process. The discretization of the heat conduction equation is performed following the finite-volume method. In this approach, the solution domain is divided into a set of discrete and nonoverlapping elements or control volumes, each associated with a grid point located at its geometric center. The discretization process is a two-step procedure. In step 1, the equations are integrated over a control volume to obtain a discretized description of the conservation laws. In step 2, an interpolation profile is used to relate some of the discretized terms from step 1 to the discrete nodes in the solution domain.

To perform step 1, Eq. (1) or (2) (with the subscript s or m dropped) is integrated over a control volume with the flux components transformed into surface integrals using Green's theorem [16]. This procedure yields

$$\int_V \frac{\partial(\rho c T)}{\partial t} dV = \oint_{\partial S} (k \nabla T) dS \quad (7)$$

The discrete form is obtained by replacing the surface integrals of the flux terms by discrete summations over the faces of the control volume, and the volume integral by the product of the integrand at the cell center and the cell volume. Upon substitution into Eq. (7), the resulting discrete equation is written as

$$\frac{\partial(\rho c T)}{\partial t} V_P - \sum_{f=nb(P)} \Gamma \nabla \mathbf{T}_f \cdot \mathbf{S}_f = 0 \quad (8)$$

where \mathbf{S}_f represents the surface area of the control volume face f and $nb(P)$ the faces of cell P .

In step 2, Eq. (8) is transformed into an algebraic equation with the time derivative approximated using an Euler-implicit formulation to yield

$$\frac{\partial(\rho c T)}{\partial t} V_P = \frac{(\rho c T)_P - (\rho c T)_P^o}{\Delta t} V_P \quad (9)$$

Moreover, the diffusion flux of T through the control volume face f can be written as

$$(-k \nabla T)_f \cdot \mathbf{S}_f = (-k \nabla T)_f \cdot \mathbf{E}_f + (-k \nabla T)_f \cdot \mathbf{T}_f \quad (10)$$

where the two vectors \mathbf{E} and \mathbf{T} satisfy the relation $\mathbf{S} = \mathbf{E} + \mathbf{T}$, with \mathbf{E} being collinear with \mathbf{d}_{PF} , the vector joining the grid points P and F straddling the control volume face (Fig. 2). The first term on the right-hand side of Eq. (10) represents a contribution similar to the one obtained on orthogonal grids (i.e., involving T_F and T_P), while the second term on the right-hand side is called cross diffusion or nonorthogonal diffusion and is due to the nonorthogonality of the grid system. Several options are available for the decomposition of \mathbf{S} . The over-relaxed approach, in which \mathbf{T} is selected to be perpendicular to \mathbf{S} (i.e., $E = S / \cos \theta$, θ being defined in Fig. 2 and E and S are the magnitudes of \mathbf{E} and \mathbf{S} , respectively), is found to be the most stable even when using highly distorted grids. In this approach, the importance of the term involving T_P and T_F increases with increasing grid nonorthogonality. For an orthogonal grid, all variations yield the same numerical discretization. Expanding Eq. (10) using a fully implicit scheme in time, the expression for the diffusion flux becomes

$$(-k \nabla T)_f \cdot \mathbf{S}_f = -k_f \left(\frac{T_F - T_P}{d_{PF}} \mathbf{E}_f + (\nabla T)_f \cdot \mathbf{T}_f \right) \quad (11)$$

where E_f is the magnitude of \mathbf{E}_f , and the cross-diffusion term is treated as a source term in a deferred correction manner, with its value computed explicitly using the current T field. By substituting Eqs. (9) and (11) in Eq. (8), the following algebraic equation is obtained:

$$(a'_P + a''_P) T_P + \sum_{F=NB(P)} a''_F T_F = a'_P T_P^0 \quad (12)$$

where the superscripts t and D indicate coefficients obtained from the discretization of the transient term and of the diffusion fluxes, respectively, and the superscript 0 designates a value from the previous time step.

To improve the robustness of the solution procedure, which is iterative in nature, the equations are usually under relaxed. Denoting the under relaxation factor by urf, Eq. (12) becomes

$$\left(\frac{a'_P + a''_P}{\text{urf}} \right) T_P + \sum_{F=NB(P)} a''_F T_F = a'_P T_P^0 + \left(\frac{1 - \text{urf}}{\text{urf}} \right) (a'_P + a''_P) T_P^{(n)} \quad (13)$$

where the superscript (n) refers to values taken from the previous iteration. This equation can be rewritten as

$$a_P T_P + \sum_{F=NB(P)} (a_F T_F) = b_P \quad (14)$$

with the coefficients given by

$$a_F = -k_f \frac{\mathbf{E}_f}{d_{PF}} \quad a_P = a'_P - \sum_{F=NB(P)} a_F$$

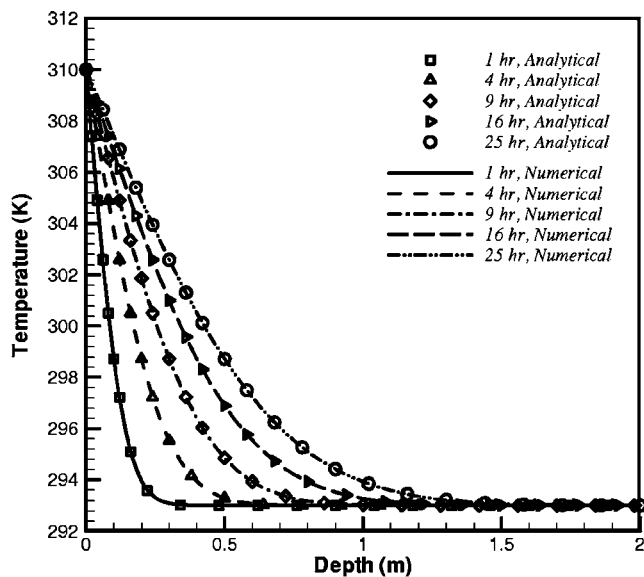
$$b_P = a'_P T_P^0 + \left(\frac{1 - \text{urf}}{\text{urf}} \right) (a'_P + a''_P) T_P^{(n)} + \sum_{f=nb(P)} (k \nabla T)_f \cdot \mathbf{T}_f \quad (15)$$

The system of algebraic equations is solved iteratively using a line-by-line tri-diagonal matrix algorithm [16]. Moreover, grid networks are generated using the transfinite interpolation technique [17]. Furthermore, since a conservative scheme is used, arranging the control volume face to coincide with the mine interface ensures energy balance at the mine-soil surface of contact [16] and forces Eq. (3b) to be satisfied identically.

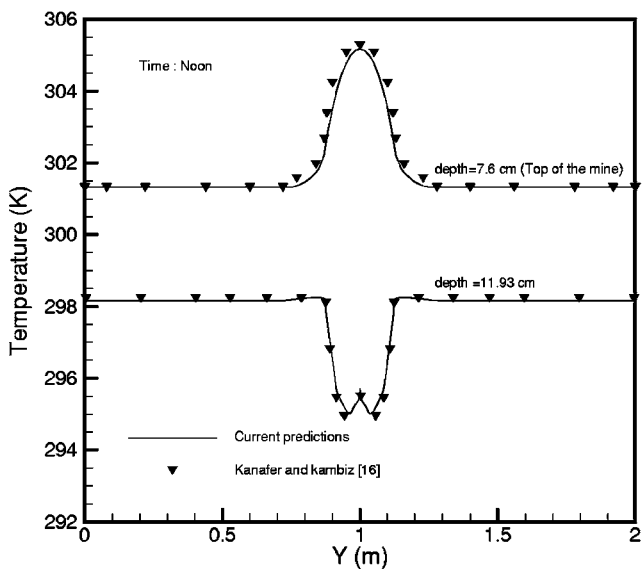
3.2 Validation of the Thermal Model. The above-described numerical procedure was implemented in a finite volume code and validated by solving several problems of which two tests are presented next.

3.2.1 Test 1: Temperature Distribution in a Semi-Infinite Wall. A soil column of depth 2 m represents the semi-infinite wall, with the soil having a density of 2000 kg/m³, a thermal conductivity of 2.511 W/m K, and a heat capacity of 837.2 J/kg K as used by Khanafer and Vafai [12]. Initially, the soil is maintained at a uniform temperature of value 293 K. At time $t > 0$, the surface temperature of the soil is increased to 310 K and the temporal evolution of temperature profiles in the soil are predicted using the developed numerical code. Predicted profiles after 1, 4, 9, 16, and 25 h are compared in Fig. 3(a) against the exact analytical profiles, assuming that heat flows in the vertical direction only. As shown, the numerical code reproduces accurately the analytical profiles, with numerical predictions falling right on top of analytical values. This is an indication of the correct implementation of the unsteady and conduction terms in the governing equation.

3.2.2 Test 2: Reproduction of Khanafer and Vafai [16] predictions. As a further check for accuracy, soil temperature profiles in the presence of a buried landmine reported by Khanafer and Vafai [12] following a finite-element approach were repro-



(a)



(b)

Fig. 3 A plot showing (a) comparison of soil temperature profiles generated numerically and analytically for the semi-infinite heat conduction problem, (b) comparison of predicted soil temperature profiles in the presence of a buried mine against those reported by Khanafar and Vafai [12]

duced. The simulated mine radius and height in the study were 0.125 m and 0.0833 m, respectively. The properties used in their work were: Trinitrotoluene (TNT) thermal conductivity = 0.22344 W/m K, soil thermal conductivity = 2.5 W/m K, soil density = 2000 kg/m³, and soil heat capacity = 837 J/kg K. Computations were repeatedly performed while refining the mesh and varying the time step until a grid and time step independent solution was reached. Predicted temperature profiles at two depths of 0.076 m and 0.1193 m are compared against similar results reported in [12]. As depicted, predictions are in good agreement with each other. The slight difference in values is attributed to some error introduced while extracting data from small figures for comparison and to the different mesh and time step used. A fixed

time step of 30 s is used in this work, while Khanafar and Vafai [12] used a variable time step with a minimum value of 0.36 s.

4 Experimental Methodology

As mentioned earlier, the current work is the first foundation in a large-scale project aiming at developing an IR-based system for the detection of buried landmines. The objective of this phase is to develop the numerical model that will be used in generating a database against which infrared images will be compared for inferring the presence or non-presence of landmines. Therefore, it is essential for this tool to be capable of generating accurate predictions. Furthermore, to fine tune the model, it is necessary to compare numerical predictions against experimental data. Recording these measurements in outdoor conditions requires accurate weather and solar radiation data. To reduce the complexity of the problem and validate the numerical tool, indoor experiments were conducted at controlled temperature and humidity conditions inside an environmental chamber. The soil surface was exposed to radiant heat flux for a short period of time and the thermal response of the soil surface as well as the inner shallow layers of the soil were monitored while cooling.

The environmental chamber has the dimensions of 3.2 m × 4.2 m × 2.8 m and is equipped with two independent systems for controlling the air temperature and relative humidity. The precision in the set conditions of the environmental chamber is ±0.5°C for temperature and ±2% for relative humidity. The test bed (width: 1 m, length: 1 m, and height: 0.65 m, see Fig. 4) placed inside the chamber is made of a 2 cm thick layer of plywood and is filled to the top with a homogeneous soil that is typically found in Lebanon and is composed of clay silty sand: 80% sand (fine), 12% silt, and 8% clay. The bed size was chosen based on preliminary numerical calculations to make sure that the boundary conditions along the sides of the bed do not affect the solution around the mine. The soil was sifted and cleaned from clutter and pebbles and its surface was carefully leveled. The measured soil density and specific heat were found to be $\rho_s = 1430 \text{ kg/m}^3$, and $C_s = 750 \text{ J/kg K}$, respectively. The soil thermal conductivity, measured using a Hilton Thermal Conductivity Unit TCU 100 of Heat Technology that does the analysis according to ISO 8301 [18], was found to be $k_s = 0.30 \pm 0.003 \text{ W/m K}$. On the other hand, at the porous surface layer, the soil thermal conductivity was measured to be $k_s = 0.25 \pm 0.003 \text{ W/m K}$. These measurements were performed on soil samples that were initially dried in a furnace.

Figure 4 shows the physical dimensions of the soil bed, the embedded mine, and the radiation source. The soil surface is exposed to radiant heat flux for a short period and then thermal signatures are observed while cooling takes place. The intention of the experiment is to understand the mechanism by which the thermal signature is induced and to develop and validate a numerical model capable of accurately predicting the mine's signature rather than simulate the actual diurnal heating and cooling cycle. The radiant heating source is composed of a set of six halogen lamps rated at 1000 W each (1 m × 1 m) placed horizontally above the soil bed at a height of 1 m and backed with parabolic reflectors. The power input to the lamp is monitored for stable nonfluctuating operation. The arrangement of the radiant lamps resulted in a nonuniform incident radiation on the soil surface. A special CM3 Campbell Scientific Pyranometer of spectral range 305–2800 nm is used to measure the radiative heat flux from the Halogen lamps at different locations on the soil surface using a grid of 0.05 m × 0.05 m resulting in 400 readings. The spectral selectivity of the pyranometer is ±5% (350–1500 nm), with a sensitivity of 10 $\mu\text{V/Wm}^{-2}$ to 35 $\mu\text{V/Wm}^{-2}$ and impedance of 60 Ω to 200 Ω . The measured reflected flux from the soil surface amounted to about 20% of the incident flux. The radiant heat flux at the surface ranged from 2052 W/m² to 2187 W/m² in the middle of the test bed region of area 0.3 m × 0.3 m. The unifor-

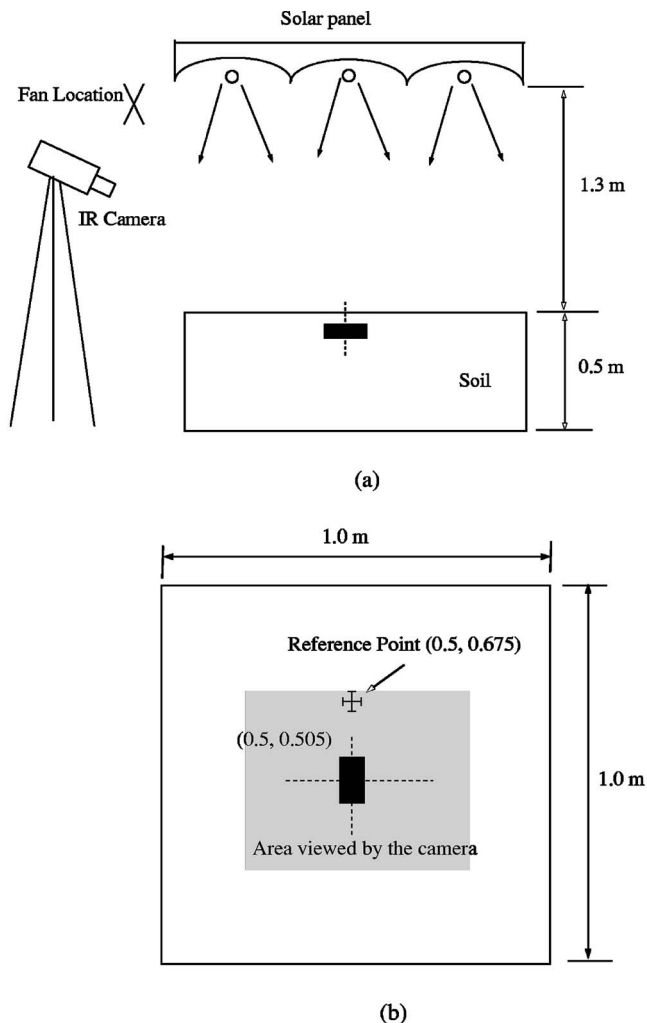


Fig. 4 A schematic of (a) the side view of the experimental setup and (b) the top view of the soil bed

mity of the radiation intensity at the soil surface is dependent on the height of the source lamps above the bed. A height of 1 m was found to give reasonable spatial uniformity on the surface above the buried mine and sufficient intensity of the radiant flux to generate realistic temperature changes on the surface and in the soil layer above the mine. Surface drying of the soil was not a problem since the thermal signature was observed during the cooling period when surface temperatures of the soil was less than 35°C. In addition, the variation of the relative humidity in the chamber was monitored to remain at 50% ± 2%. The continuous renewal of the air during cooling in the chamber maintained steady temperature above the soil bed.

The mine is embedded in the soil at a distance $x=0.5$ m and $y=0.505$ m from the origin of the bed, located on the lower left-hand corner. This location is selected so that the surface of soil above the mine is well within the view of the IR camera and is exposed to spatially uniform radiative flux during the heating period. A common type of antipersonnel mine of rectangular shape (13.9 cm × 5.4 cm × 6.7 cm) is used. The mine is filled with (RTV) material that has properties similar to TNT (specific heat $c_m=1500$ J/kg K, thermal conductivity $k_m=0.2$ W/m K, and density $\rho_m=1170$ kg/m³) and is buried in the soil. The plastic cover of the mine has a thickness of 0.3 cm, specific heat $c_p=1260$ J/kg K, thermal conductivity $k_p=0.5$ W/m K, and density $\rho_p=1760$ kg/m³. The burial depth is an experimental parameter and is varied from 0.5 cm to 2.5 cm.

Two measurement methods are used in this work. The main measurement instrument is the IR ThermoCAM S60 camera (7.5–13 μm spectral range), which has a temperature sensitivity of 0.08°C at 30°C and accuracy of ±2% of reading. The camera is air-cooled and tower mounted horizontally at a height of 0.6–1 m from the soil surface. A tripod mounted IR camera, at a lens-to-soil distance of 1 m angled at 45° from the horizontal, is utilized to capture images of the soil surface at the peak, when a significant variation in temperature is noted. The capture card employing the ThermoCam Professional 2.8 [19] software stores images (joint photographic experts group (JPEG) and Microsoft bitmap format (bmp)) and videos taken by the camera. The surrounding air temperature (level temperature) and the distance between the lens and the object are adjusted in the camera and autozoom is used. A major challenge in the work is processing the acquired images with a high degree of accuracy. Because IR sensors are passive sensors that quantify emitted infrared radiation from a body surface, the radiation measured by the camera is not only dependent on the temperature of the body, but it is also a function of the emissivity of the surface. This is why the emissivity setting of the camera significantly affects the accuracy of the measured temperature differences. To minimize error, the soil emissivity was carefully measured following two different procedures and was found to be equal to 0.92. Another input parameter was the reflected temperature, which was equal to the ambient temperature in an outdoor environment and takes into consideration the radiation from the surroundings reflected via the object surface to the camera. When reflected temperature input to the camera increased, the absolute temperatures decreased, but the difference in temperature between any points on the surface remained unchanged. The surrounding objects in the climatic chamber were all set at the ambient temperature with the exception of the halogen lamps panel. Since the solar panel is highly reflective and has a very low emissivity, the camera reflected temperature was put equal to the chamber air temperature. The camera resolution is 320 × 240 pixels capable of registering data at 76 800 pixel locations on the surface.

The second technique involves using K-type thermocouples to measure soil temperature with an accuracy of ±0.5°C. Thermocouples, mounted on a glass rod at the reference location ($x=0.675$ m, $y=0.505$ m) were positioned at depths of 0 mm, 4.5 mm, 10.5 mm, 18 mm, and 45 mm. The thermocouples tips were not bonded to the rod, but were stuck out at a distance of at least 10 mm from the rod surface into the desired soil locations to eliminate the effect of the glass rod conductivity on the readings. Additional thermocouples were located at the center of the mine's top surface and the soil's surface above the mine center. The soil surface temperature was monitored at the sensors reference location using a special temperature probe Model 108 Campbell Scientific with a resolution of ±0.3°C over the range -3°C to 90°C. In addition, a precision infrared temperature sensor (IRTS-P) is positioned 0.5 m above the bed corner directed toward the soil surfaces above the center of the buried mine. The IRTS-P sensor has a silicon lens whose field of view is a circle of 1 m diameter when the sensor is 3 m away from the target. To accurately process infrared images, the air temperature and relative humidity above the soil bed were monitored. All thermocouples were calibrated before the start of the tests and were connected to a Campbell Scientific CR23X logger capable of recording one set of readings per second. Sampling of the temperature readings was done every 10 s. A small fan was placed parallel to the heater and away from the soil bed, at the heating panel level of 1 m, to accelerate cooling by increasing convection heat transfer. The air speed at a height of 1 m was measured using a handheld airflow meter and was found to be equal to 4.5 m/s ± 0.1 m/s.

The soil bed was conditioned inside the environmental chamber at an air temperature of 25°C and relative humidity of 50% for at least 48 h for steady state to be reached. Following this conditioning period, the soil surface was heated for five minutes, after

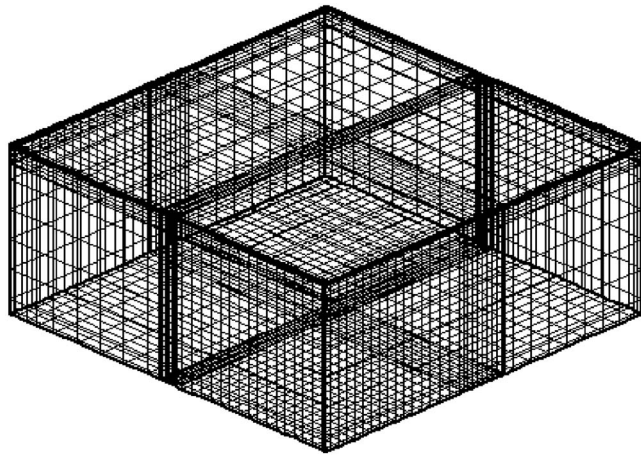


Fig. 5 The computational domain

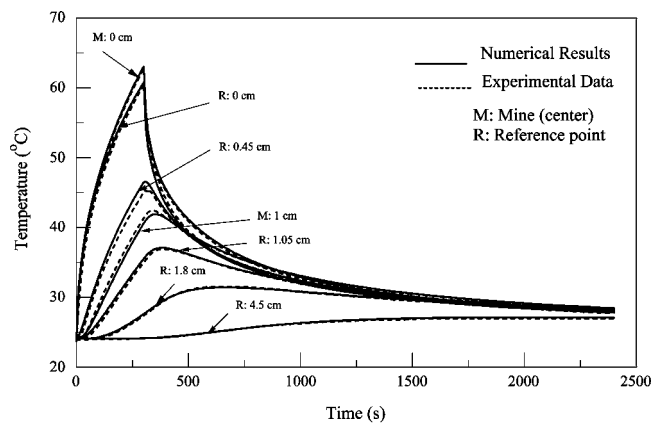
which the heat source was stopped and images of the soil surface were taken at one-minute intervals to monitor the surface temperature changes during the cooling period. The tests were performed with the fan either on or off to study both forced and natural convection cooling, respectively. The experiments were carried out with a mine buried at predetermined depths to examine the surface signature changes during cooling using the IR camera and while recording temperature readings at the surface above the mine and at the reference point location and in depth. The air temperature in the environmental chamber was monitored at four different locations.

For natural cooling, the air temperature above the soil increases by about 5°C from its initial value (the heating period is 5 min), but cools quickly to the chamber temperature within the first five minutes after shutting off the heat source. When repeating the test with the fan turned on, the temperature of the air above the soil increases by 2.5°C only for the same heating period. The interval between any two experiments is at least 48 hours to allow the soil and the environmental chamber air to reach thermal equilibrium as this condition is important for the numerical simulation.

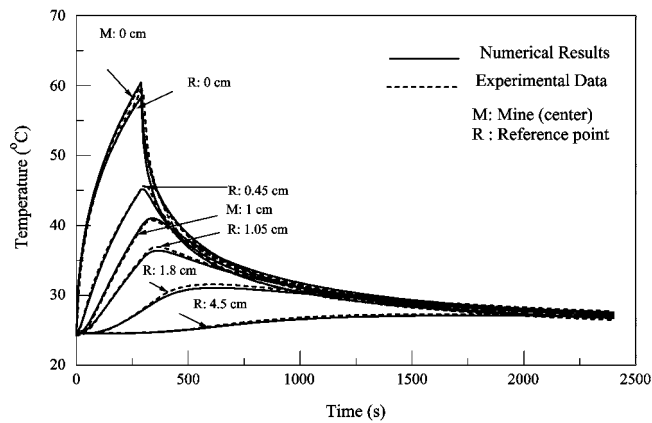
5 Result and Discussions

5.1 Experimental Results and Validation of the Numerical Thermal Model. The use of a three-dimensional conduction model was dictated by the non-uniform heating of the soil surface in the experiments, the geometry of the mine, and the willingness to validate such as model as it will be used for developing an IR-based tool for detecting buried landmines.

Before comparing numerical results to measured values, the grid and time step were adjusted until a grid and time step independent solution was obtained. This was accomplished with an $80 \times 80 \times 54$ grid network with the grid points nonuniformly distributed as shown in Fig. 5 using a time step of 10 s. All results presented here were generated using the aforementioned grid system and time step for the physical domain described in the experimental section and using the measured thermal properties of the soil, mine and RTV filling material ($\rho_s = 1430 \text{ kg/m}^3$, $c_s = 770 \text{ J/kg K}$, $c_m = 1500 \text{ J/kg K}$, $k_m = 0.2 \text{ W/m K}$, density $\rho_m = 1170 \text{ kg/m}^3$). The spatially varying heat flux on the soil surface, needed as a boundary condition in the numerical simulations, was calculated at the center of each control volume by interpolating between the nearest two or four experimentally measured incident heat flux values. These interpolated estimates were assumed to prevail over the entire control volume face. The initial temperature of the soil was set equal to the temperature of the ambient air in the environmental chamber. Results are presented for the two methods of cooling by forced and natural convection. Tests were carried out using a rectangular shaped mine filled with RTV ma-



(a)



(b)

Fig. 6 The variation in time of the predicted and measured temperatures at the center of the mine surface at $z=0.01 \text{ m}$, and the soil surface at the reference point at depths of 0.45 cm, 1.05 cm, 1.8 cm, and 4.5 cm for a test conducted in the environmental chamber while heating the soil bed for a period of 5 min and then cooling by (a) radiation and forced convection with the fan turned on and (b) radiation and natural convection with the fan turned off

terial buried at depths of $z=0.5 \text{ cm}$, 0.75 cm , and 1 cm from the surface at $x=0.5 \text{ m}$ and $y=0.505 \text{ m}$. The reference point at which temperature values are recorded corresponds to the location $x=0.675 \text{ m}$ and $y=0.505 \text{ m}$. The environmental chamber is set to 25°C and 50% relative humidity.

Figure 6 shows the temporal variation of the predicted and measured temperatures at the center of the top surface of the mine ($z=1 \text{ cm}$), the soil surface above the center of the mine, and the reference point at depths of 0.45 cm, 1.05 cm, 1.8 cm, and 4.5 cm for two test cases. Heating of the soil surface in both configurations took place over a period of 5 min. The difference between the two situations is in the cooling method, which occurred either with the fan turned on (Fig. 6(a)) or off (Fig. 6(b)). As shown in Figs. 6(a) and 6(b), the soil surface temperature is less sensitive to changes in the convection heat transfer coefficient during the heating period since the heat gain by radiation in that time interval is at least one order of magnitude higher than the convection heat loss. After turning off the lamps, the surface cooling rate shows a steep gradient indicating immediate response with its temperature dropping sharply. Comparing profiles in Figs. 6(a) and 6(b) it is noticed that the value of the convection heat transfer coefficient affects the cooling rate, but does not affect the time of peak at any depth z in the soil. Due to storage effects, the time at which the temperature peaks, for both methods of cooling, increases with

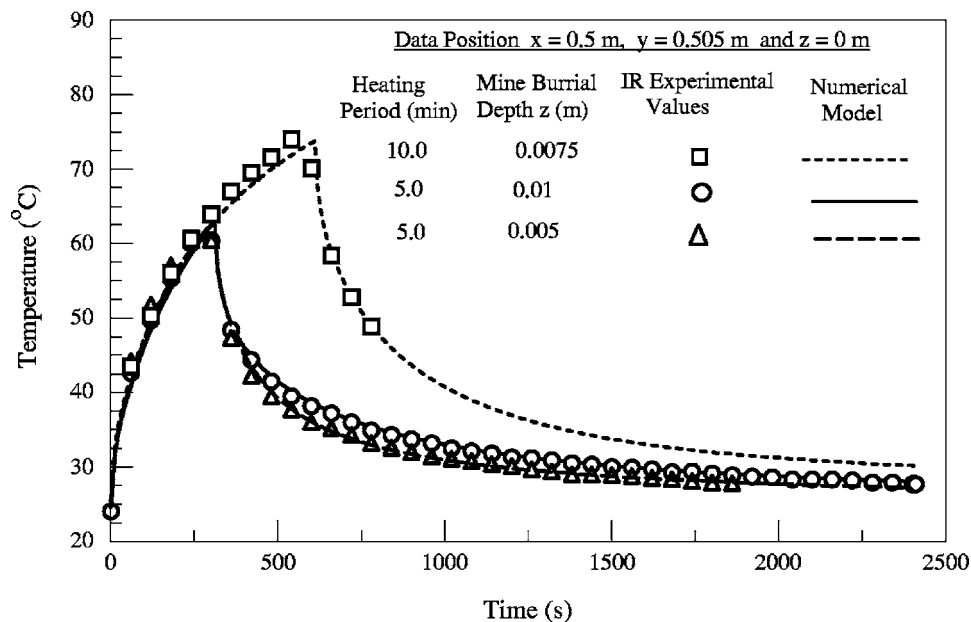


Fig. 7 The test results of the soil surface temperature above the mine center predicted by the numerical model and measured by the infrared camera at 1 min intervals for a mine burial depths of 0.005 m, and 0.01 m with a heating period of 5 min and a burial depth of 0.0075 m with a heating period of 10 min

depth. The numerical model is able to reproduce the actual thermal processes that take place in the soil since temporal temperature profiles obtained near the surface and inside the soil are in excellent agreement with measurements. The maximum error is less than 4% between the measured and numerically predicted values. This agreement was achieved after rigorous experimentation and sensitivity analysis of the effect of the various physical parameters on the predicted response. Initially, even though solutions were close to measurements below the surface, it was not possible to match it at the surface. The extensive analysis performed identified the soil thermal conductivity in the layer close to the surface to be the cause. Due to continuously disturbing the soil while setting up the experiment, the soil in the layer close to the surface has more air void than deeper soil. Therefore, the thermal conductivity of the surface layer is different from the measured soil value and has to be calculated as a weighted average of the thermal conductivities of the soil and air. This conclusion was verified experimentally using a portable Quicktime30 Thermal Properties Analyzer (the device has an accuracy of 5% or ± 0.001 W/m K for thermal conductivity in the range of 0.05–0.7 W/m K). The same situation would be faced with a newly buried landmine. For the conditions of the experiment, the value measured by the device helped developing the following equation for the soil thermal conductivity, which was used within the top 1 cm of the soil bed:

$$k_{s,\text{surface}} = k_s \left(1 - \frac{e^{-3z}}{6} \right) \quad (16)$$

where $k_{s,\text{surface}}$ is the soil thermal conductivity at depth z (expressed in centimeters) and k_s is the soil thermal conductivity. As depicted in Figs. 6(a) and 6(b), the use of Eq. (16) allowed accurate numerical predictions of the soil surface response while also predicting accurately the soil thermal response in depth. Moreover, the interface of the plastic layer surface of the mine box is not ideal due to the porous characteristics of the soil. A thin interface air layer of 0.03 mm thickness was used between the plastic cover of the mine, which has a thickness of 0.1 mm, and the soil. The thin interface layer introduced in the solution represents a physical effect resembling the contact resistance between the sand

and the plastic rigid surface and is different than the top air gap region within the mine cover in the work of Khanafer and Vafai [12] of 10 mm thickness compared to the interface layer outside the plastic cover of 0.3 mm used in this work. The predicted soil surface temperature above the mine and on the mine center agrees well with experimentally measured values using thermocouples.

Figure 7 presents a comparison between numerical predictions and measurements taken by the infrared camera at 1 min intervals for the soil surface temperature above the mine center for burial depths of 0.005 m and 0.01 m when the heating period is 5 min and of 0.0075 m when the heating period is 10 min. Good agreement is observed where differences between readings and predictions is less than 0.3°C. The longer heating period results in higher surface temperatures and a faster cooling rate of the soil. The experiments have been limited to shallow burial depths due to the limitations imposed by the heating source strength and the type of soil which has a close thermal conductivity (0.25–0.3 W/m K) to the buried RTV material in the mine (0.2 W/m K). Typical soil conductivities that appeared in other studies ranged from 0.5–0.75 W/m K and have shown ability to detect signatures up to 2–5 cm depth in outdoor tests [12,14]. Further processing of surface images taken by the infrared camera will assess the thermal contrast between the surface temperature measured above the mine and at a point away from the mine.

6 Analysis of Thermographic Results and Image Processing

The output of the IR camera is a JPEG image with its temperature palette. An algorithm was developed to map the captured pixels' attributes to absolute temperatures. The input for this algorithm is the IR image and its color temperature palette, while the output is a set of temperature values. Figure 8(a) shows the reference spatial extent of the camera image, an actual image showing the mine signature, and the temperature distribution along a line on the surface of the soil for the experiment whose data are presented in Fig. 6(a). Figure 8(b) shows the three-dimensional temperature distribution on the surface as generated by the mapping algorithm from the IR images at 5 min and 10 min from the

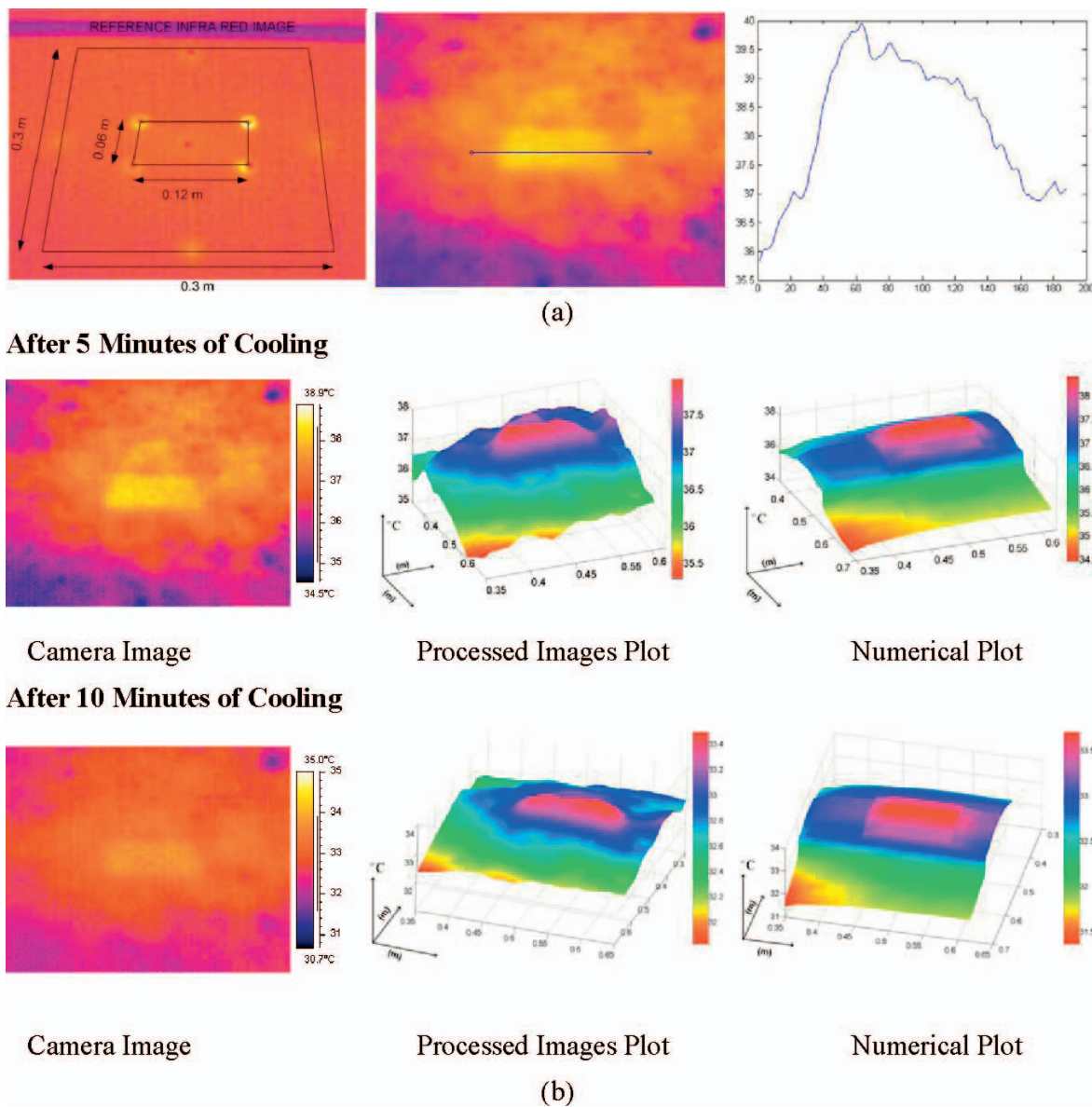


Fig. 8 (a) The soil bed reference image at steady conditions of the environmental chamber, and the IR camera image during the cooling period, and the temperature distribution plot along a line on the surface of the soil for the experiment whose data were discussed and shown in Fig. 6(a); (b) the IR camera image, the 3-D temperature distribution of the surface as generated by the mapping algorithm from the IR images at 5 min and 10 min from the onset of cooling, and the corresponding surface images generated by the numerical model. (Heating period =5 min, mine depth=0.01 m, $T_{\infty}=25^{\circ}\text{C}$, RH=50%.)

onset of cooling and the corresponding surface images generated by the numerical model. The mean difference in temperature values between the camera images and those produced by the numerical code is less than 0.2°C while the maximum difference is 0.3°C . The spatial nonuniformity in the camera image is due to the incident nonuniform flux from the heating lamps during heating.

The thermal signature or contrast is defined in this work as the temperature difference between the point on the soil surface above the mine center and the reference point. For the results discussed earlier, the numerical and experimental thermal contrasts were calculated and their values, denoted by TC'_{\max} , were found to represent the maximum possible temperature difference on the soil surface. Figure 9 shows the predicted thermal contrast, and the measured thermal contrast using the IR images and the thermocouples' readings as a function of time for (a) mine burial depth

of 0.005 m (5 min heating), and 0.0075 m (10 min heating) and (b) mine burial depth of 0.01 m (5 min heating). The first is for a mine buried at 0.005 m under the surface and exposed to 5 min of heating and the other is for a mine buried at 0.0075 m and exposed to 10 min of heating. The shallower mine has given a peak contrast of about 4°C after one minute from the start of the cooling process, while the deeper mine has given a maximum contrast of 3.5°C directly at the end of the heating period. The time of occurrence of the peak contrast depends on both the mine depth and the heating period. The difference in temperature between the numerical and experimental readings is less than $\pm 0.3^{\circ}\text{C}$ during cooling, while during heating the error is slightly higher ($\pm 0.5^{\circ}\text{C}$) due to the sensitivity of the camera to the surface temperature and the need to adjust its range for temperatures above 60°C . The camera images produce more accurate readings of the surface

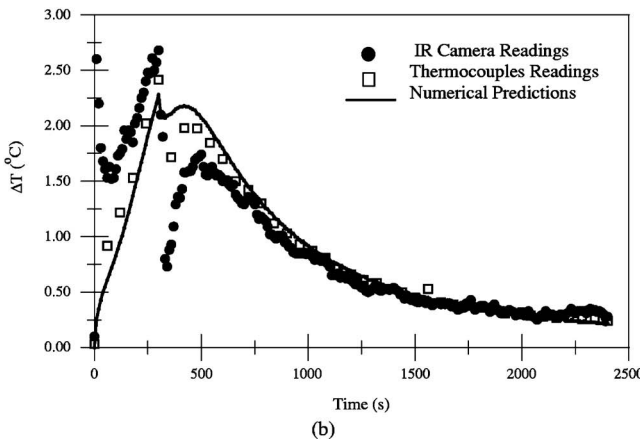
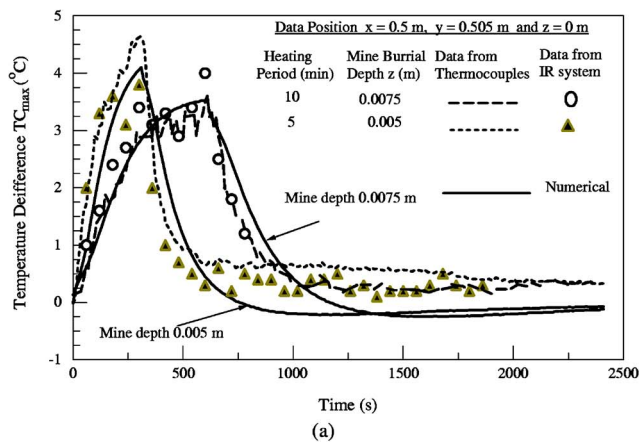


Fig. 9 A plot of the predicted thermal contrast, and the measured thermal contrast using the IR images and the thermocouples' readings as a function of time for (a) burial depth of 0.005 m (5 min heating), and 0.0075 m (10 min heating) and (b) burial depth of 0.01 m (5 min heating)

temperature than the thermocouple particularly in the period when heating source is turned off. The surface of the soil is rough and the tip of the thermocouple is in touch with the air and the soil grain. At the end of the heating period, the soil temperature is not in equilibrium with the air temperature in the void space of the soil. This causes a drop in the measured temperature at that instant given an error of about 0.7°C due to the sudden change from heating to cooling at the surface.

For fixed thermal properties of soil and mine material, the dependence of the peak thermal contrast on time, depth, and heating period was investigated numerically. Figure 10 shows plots of the thermal contrast as a function of time for (a) a heating period of 5 min. (b) a heating period of 20 min at different mine depths, and (c) different heating periods at fixed mine depth. Plots in Figs. 10(a) and 10(b) indicate that the thermal contrast decreases with increasing mine's burial depth. On the other hand, Fig. 10(c) reveals that the peak thermal contrast does not change when the heating period increases beyond 10 min. Figure 11 presents the variation with depth of (a) the peak thermal contrast and (b) the time of the peak occurrence for heating periods of 5 and 20 min. As shown in Fig. 11(a), the value of the peak thermal contrast increases with the heating period due to the larger amount of energy stored in the soil during heating. However, Fig. 11(b) indicates that the time of occurrence of the peak thermal contrast increases with depth and approaches the end of the heating period.

The numerical method has predicted well the transient thermal response of the soil surface and the resulting thermal signature. Integrating the model with an IR imaging system will help iden-

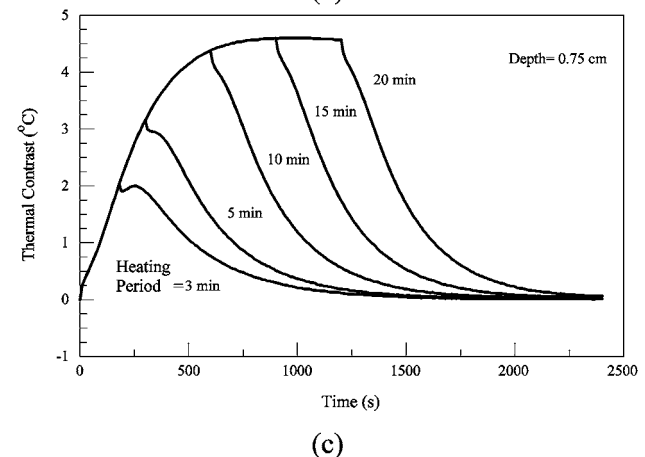
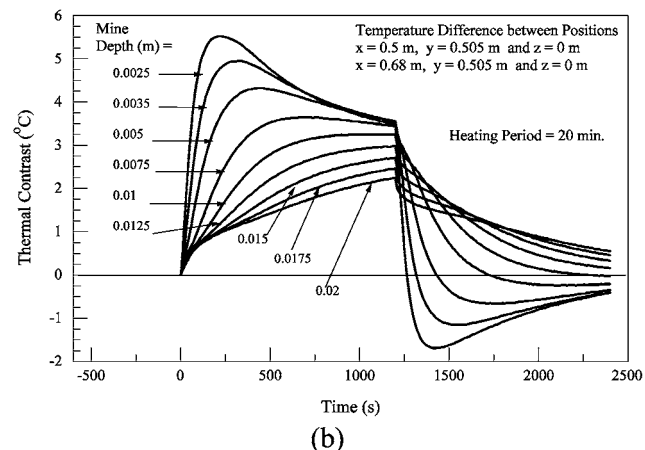
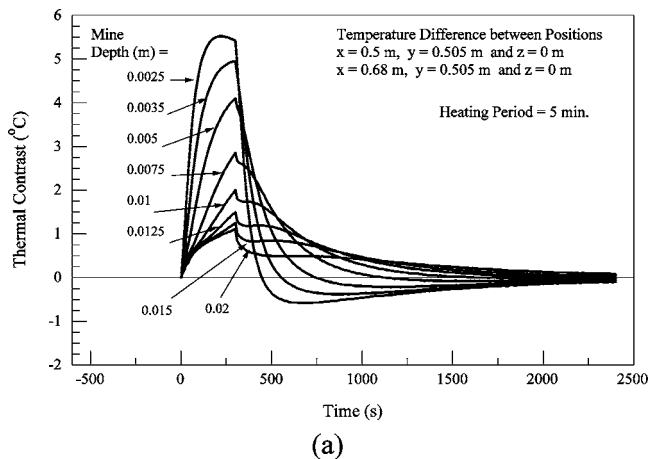


Fig. 10 A plot of the thermal contrast as a function of time for (a) a heating period of 5 min, (b) a heating period of 20 min at different mine depths, and (c) different heating periods at fixed mine depth for the same climatic conditions of the indoor experiments considered in this work

tifying potential target objects. In the real situation, the mine location is not known a priori. Moreover, relying on the experimental data is not enough neither to identify the targets nor to determine their depths if classified as mines. However, using the numerical model it is possible to generate a database of solutions against which real images can be compared. The thermal signature maps of the database at the different periods can then be used to aid classifying the target. Among other objectives, future work will be directed toward developing a criterion that transforms the

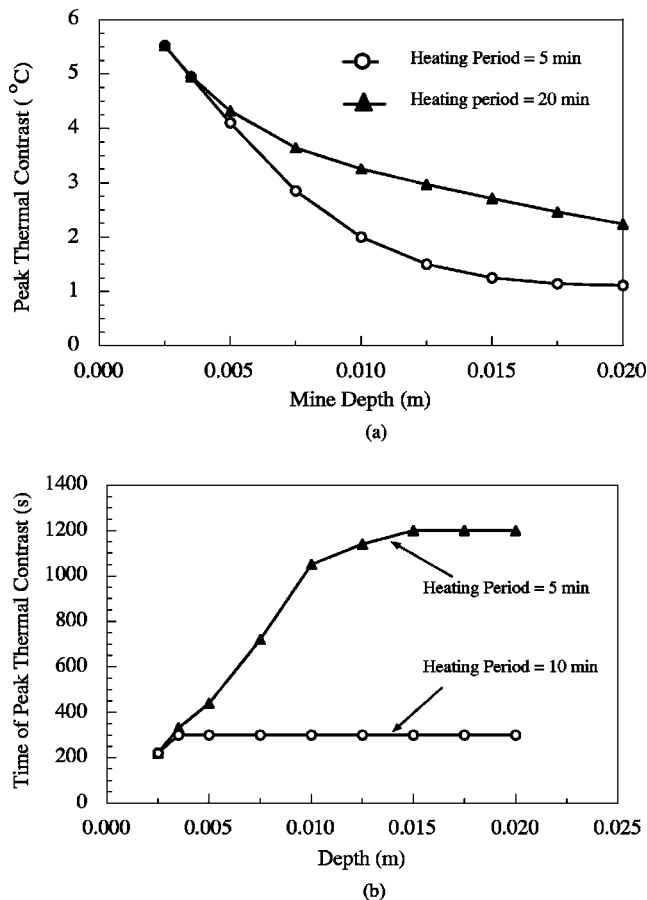


Fig. 11 The variation with depth of (a) the peak thermal contrast and (b) the time of the peak occurrence

information contained in the thermal contrast maps into decision indices that help identifying targets with precision and reduce false alarms.

7 Conclusion

A three-dimensional finite volume simulation tool for the prediction of buried landmines in dry soil has been developed. The numerical model was validated by comparison with published data and by experimentation. The model predicts the expected soil thermal signatures evolving due to the presence of buried objects. The generated numerical results match with high accuracy the experimentally generated IR images of the soil surface when subjected to heating and cooling. The key element in matching experimental and numerical images stems from the consideration of the change in thermal conductivity of the soil from surface and shallow surface values to higher value at more depth. The thermographic analysis of the model and IR images will further be developed to produce additional information that can help in classifying the detected objects.

Acknowledgment

The authors acknowledge the support of the Lebanese National Council for Scientific Research Grant No. LCR-11304-002208. In addition, the authors would like to acknowledge the support of Youssef Jameel Grant for acquisition of the IR camera, sensors, and support to graduate students. The environmental chamber lab facility is supported by the American School and Hospital Aid (ASHA) Grant No. AUB-FEA-793. The help of the research engineer, Samir Berjaoui in performing the sensitivity analysis, cali-

brating the sensors, and conducting the experiments is highly appreciated.

Nomenclature

- a_p, \dots = coefficients in the discretized equation
- b_p = source term in the discretized equation
- k = thermal conductivity (W/m K)
- urf = under-relaxation factor
- \mathbf{S}_f = surface vector
- t = time (s)
- T = temperature (°C)
- \mathbf{n} = outward unit vector normal to cell face
- \mathbf{d}_{PF} = vector joining the grid point P and F
- \mathbf{E} = vector collinear with \mathbf{d}_{PF}
- \mathbf{T} = vector equals to $\mathbf{S}-\mathbf{E}$
- C = specific heat (J/kg K)
- V = volume of control cell
- h = heat transfer coefficient (W/m² K)
- A = surface area of soil (m²)
- q = heat flux (W/m²)
- x, y, z = rectangular coordinate system

Greek Symbols

- ρ = density (kg/m³)
- Δt = time step (s).
- σ = Stefan-Boltzmann constant (W/m² K⁴).
- ε = emissivity.

Subscripts

- f = refers to control volume face f
- P = refers to the P grid point
- F = refers to the neighbor of the P grid point
- ∞ = refers to ambient conditions
- s = refers to soil
- m = refers to mine
- net = refers to net heat flux at soil surface
- conv = refers to convection heat flux at soil surface
- rhs = refers to incident radiation heat flux on soil surface
- emis = refers to emitted heat flux from soil surface
- NB = refers to the neighbors of the P grid point
- nb = refers to faces surrounding the P grid point

Superscripts

- o = refers to values from previous time step
- n = refers to values from previous iteration
- t = refers to transient contribution
- D = refers to diffusion contribution

References

- [1] Lopez, P., Sahli, H., Vilarino, D. L., and Cabello, D., 2003, "A Target Identification Procedure for the Detection and Classification of Landmines from IR images," *Proceedings of EUDEM2-SCOT-2003: International Conference on Requirements and Technologies for the Detection, Removal, and Neutralization of Landmines and UXO*, September 15–18, Brussels, Belgium, **5046**, pp. 242–252.
- [2] Simard, J. R., 1996, "Improved Landmine Detection Capability (ILDC): Systematic Approach to the Detection of Buried Mines Using IR Imaging," *Proc. SPIE*, **2765**, pp. 489–500.
- [3] Simard, J. R., 1997, "Theoretical and Experimental Characterizations of the IR Technology for the Detection of Low-Metal and Nonmetallic Buried Landmines," Centre de Recherches pour la Defense Valcartier, Quebec.
- [4] Russell, K. L., McFee, J. E., and Sirovyak, W., 1996, "Remote Performance Prediction for Infra-Red Imaging of Buried Mines," *Proc. SPIE*, **2933**, pp. 762–769.
- [5] Agrawal, S., Sriram, P., and Mitchell, R., 2001, "Algorithms for IR Imagery Based Airborne Landmine and Minefield Detection," *Proc. SPIE, Remediation Technologies for Mines and Minelike Targets VI*, **4394**, pp. 284–295.
- [6] Ngan, P., 1995, "Development of Automatic Target Recognition for Infra-Red Sensor-Based Close Range Land Mine Detector," *Proc. SPIE*, **2496**, pp. 881–889.
- [7] Bruschini, C., and Gros, B., 1998, "A Survey of Current Sensor Technology

- Research for the Detection of Landmines,” *Sustainable Humanitarian Demining: Trends*, Mid Valley Press, Verona, VA, pp. 314–325.
- [8] Deans, J., Schmithalis, G., and Carter, L. J., 2001, “An Analysis of a Thermal Imaging Method for Landmine Detection Using Microwave Heating,” *J. Appl. Geophys.*, **47**, pp. 334–352.
- [9] Hermann, J., and Ian, C., 1999, “Microwave Enhancement of Thermal Landmine Signatures,” *Proc. SPIE*, **3710**, Part I, pp. 154–166.
- [10] Mitchell, R., Srinivasa, S., and Agarwal, S., 1999, “Detection of Antipersonnel Landmines Based on Waterjet Induced Thermal Images,” *Proc. SPIE*, **3710**, Part I, pp. 180–188.
- [11] Depak, M., Agarwal, S., Ritech, G., and Swonger, C. W., 2004, “False-Alarm Mitigation and Feature-Based Discrimination for Airborne Mine Detection,” *Proc. SPIE*, **5415**, pp. 1163–1173.
- [12] Khanafer, K., and Vafai, K., 2002, “Thermal Analysis of Buried Land Mines over a Diurnal Cycle,” *IEEE Trans. Geosci. Remote Sens.*, **40**(2), pp. 461–473.
- [13] Khanafer, K., Vafai, K., and Baertlein, B. A., 2003, “Effects of Thin Metal Outer Case and Top Air Gap on Thermal IR Images of Buried Antitank and Antipersonnel Land Mines,” *IEEE Trans. Geosci. Remote Sens.*, **41**(1), pp. 123–135.
- [14] Lopez, P., Sahli, H., Vilarino, D. L., and Cabello, D., 2003, “Detection of Perturbations in Thermal IR Signatures: An Inverse Problem for Buried Land Mine Detection,” *Proceedings of EUDEM2-SCOT-2003: International Conference on Requirements and Technologies for the Detection, Removal, and Neutralization of Landmines and UXO*, September 15–18, Brussels, Belgium, **1**, pp. 385–392.
- [15] Sendur, I. K., and Baertlein, B. A., 2000, “Numerical Simulation of Thermal Signatures of Buried Mines Over a Diurnal Cycle,” *Proc. SPIE, Detection and Remediation Technologies for Mines and Minelike Targets V*, **4038**, pp. 156–167.
- [16] Patankar, S. V., 1980, *Numerical Heat Transfer and Fluid Flow*, Hemisphere Publishing, New York.
- [17] Gordon, W. J., and Theil, L. C., 1982, “Transfinite Mappings and Their Applications to Grid Generation,” J. F. Thompson ed., *Numerical Grid Generation*, North Holland, New York, pp. 171–192.
- [18] ISO 8301, 1991, Thermal Insulation, Determination of Steady-State Thermal Resistance and Related Properties,” Heat Flow Meter Apparatus.
- [19] Software 2004 “ThermaCamTM Researches Pro 2.8, Copyright©1997-2004, FLIR Systems AB.